Probing the morphology of dust particles in deep ice cores with light scattering

Llorenç Cremonesi(*)

DISAT, Università degli Studi di Milano-Bicocca - Milan, Italy

received 31 January 2021

Summary. — The size distribution and light extinction cross-section of airborne particles are among the climate proxies investigated in palaeoclimate research and required by radiative transfer models. The optical properties of the particles are acquired by a non-invasive, single-particle light scattering technique to characterise aeolian dust stored in deep polar ice core samples. The same method is applied to study alpine ice cores and firn cores. The particle-by-particle approach provides a comprehensive statistical analysis while overcoming the limitations imposed by low concentrations ($\sim 10^1$–10^3 ng/g). From a geometrical standpoint, dust particles deviate significantly from homogeneous spheres, as expected by many studies on mineral dust sources and ice core analysis. Features such as shape and structure prove to have greater importance than the particle refractive index in determining their radiative properties. By comparing experimental data to computationally inexpensive simulations, the main morphological properties of the particles can be inferred, such as the ratio between the axes in prolate particles and the porosity in isometric aggregate particles.

1. – Introduction

Even the clearest skies conceal countless particles, known as aerosols, in the nanometre and micrometre size range. Aerosols travel long distances from their sources and have a significant impact on climate on a local and global scale. For example, they serve as condensation nuclei in clouds and enhance melting in glaciers and snowpacks when deposited on the cryosphere. Moreover, their interaction with solar and terrestrial radiation makes them an important term appearing in the energy balance of the Earth [1-4]. A relevant mass contribution to the particle load in the atmosphere is due to tiny soil particles, referred to as *airborne mineral dust*, from deserts and scarcely vegetated lands. Wind

(*) E-mail: llorenc.cremonesi@unimib.it

erosion processes, saltation, and sandblasting produce micrometric and sub-micrometric mineral particles that are entrained into the atmosphere at a rate of $1-3 \cdot 10^3$ Tg/y [5,6].

A growing body of literature deals with the structure, shape, and composition of such dust particles in an effort to quantify their effect on climate, as well as their optical properties. While dielectric particles have mostly a cooling effect, strongly absorbing particles have the potential to counteract this contribution [7-12]. To this aim, many non-invasive optical techniques for characterising aerosols have been adopted or developed [13-21]. Ground-based remote sensing networks estimate the overall aerosol optical depth of the atmosphere by providing real-time monitoring of the atmospheric aerosol optical properties with a very high time resolution [22]. Conversely, an analysis on a particle-by-particle basis is preferable when investigating redeposited grains.

In the following pages, we focus on the many airborne particles once deposited on the surface of glaciers that in time, layer after layer, grow deeper. Ice cores host a footprint of the aerosol content of the past atmosphere that would otherwise be lost: this library safely stores air bubbles, dust, and other pollutants in chronological order. A remarkable variety of sources and mineralogical compositions involve the particles that can be found in any glacier, even without taking into account anthropogenic sources, soot, biomass burning, sea salt, and volcanic aerosols [23-26].

Two dominant features of fine dust aerosols are their size and mass distributions, which impact particle circulation dynamics and are required by atmospheric models [3]. Generally, the size of the particles is known to follow a log-normal distribution. Many definitions of the size of irregularly shaped particles can be devised, each giving an estimate that best suits a specific application and obtained with a different technique [27]. For example, an aerodynamic particle sizer gives the *Stokes radius*, a Coulter Counter gives the *volume-equivalent radius*, whereas an optical particle sizer based on light extinction (alternatively, the light scattered over a given solid angle) gives the *extinction radius* following a Lorentz-Mie approximation [28-31]. This ambiguity can raise some inconsistencies when comparing measurements; there is no easy answer to whether one approach should be preferred to the others, as each parameter encapsulates slightly different properties of the particles. Drag, settling, and atmospheric transport are well described in terms of the Stokes radius [32]. On the other hand, the mass distribution can be inferred by assessing the volume of the particles, whereas the single-scattering extinction cross-section gives an effective description of the contribution of mineral dust to radiative transfer [33, 34]. Here we discuss the radiative properties of the particles, which depend primarily on their size and composition. This relation is far from trivial, given that the objects under consideration are comparable in size to the wavelength or larger [35]. Furthermore, the morphology of a particle, as determined by factors such as shape, internal structure, and surface roughness, affects to the same extent its ability to scatter and absorb light (see for example [12, 14, 34, 36]). The present paper presents a brief overview of some results obtained from the analysis of liquid samples, specifically, melted ice cores containing mineral dust particles, with a single-particle optical method.

2. – Methods

In the following, we examine light scattering data from dust particles once stored in ice cores from Antarctica that date back to the Last Glacial Maximum and the Middle Pleistocene (Chibanian). Small portions of about $10 \, \text{cm}^3$ were cut and isolated in sealed plastic tubes in a cold room (-20 °C). In a clean room, we measured the extinction cross-section, C_{ext}, of individual particles suspended in water, immediately after melting
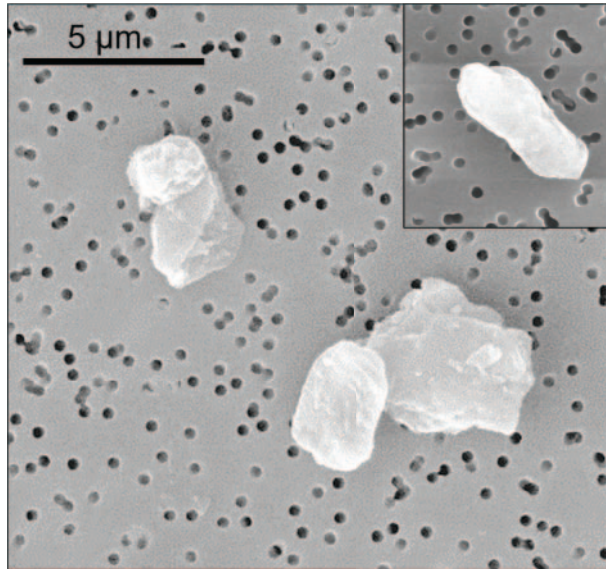
Fig. 1. – Scanning electron microscope image of micrometric mineral dust particles from a deep ice core from Dome C, Antarctica (2923.4 m deep, ∼549 ky BP).

at room temperature (24 °C) the ice that embedded them. In addition to overcoming limitations due to very low concentrations (0.1–1 ppm), choosing a particle-by-particle approach also addresses the high polydispersity of the samples. Coulter counter measurements showed that volume-equivalent diameters of the particles typically range between $0.5\,\mu$m and $4\,\mu$m, with some occurrences up to $10\,\mu$m; the presence of aggregates can cause this upper limit to exceed $20\,\mu$m. An example of some particles found in the samples is given in fig. 1. At about 3 km depth, mineral dust undergoes post-depositional aggregation, so that some of the samples contain a mixture of aggregate and compact particles [37].

We employed the Single Particle Extinction and Scattering method for the analysis, which measures the forward-scattered field, as described in detail in [38]. In addition to C_{ext}, from the forward scattering amplitude, $S(0)$, we deduce the optical thickness of each particle, ρ, related to the phase-shift of the forward-scattered field [35]. To this observable contribute several features, mainly the size and polarizability of the particle.

In principle, one may assign to (almost) any point in the (C_{ext}, ρ)-plane a sphere with a given radius and refractive index (equivalently, the complex $S(0)$ plane). However, this one-to-one correspondence is strictly limited to homogeneous, non-absorbing spheres. Since dust particles are not spherical nor homogeneous, it is not straightforward to assume any given shape for the particles or to estimate their average polarizability [36].

With the aim of using light scattering as a probe for particle morphology, we focus on some of the features resulting from particle shape rather than relying on a specific model for inverting the scattering data to give the particle size distribution. We simulated light scattering with a Discrete Dipole Approximation (DDA) algorithm, whereby to set some constraints on the geometrical parameters of the particles by comparison with experimental data. Each particle is discretised in many small sub-volumes (dipoles); the method then calculates their interaction with a given incident electromagnetic wave, including
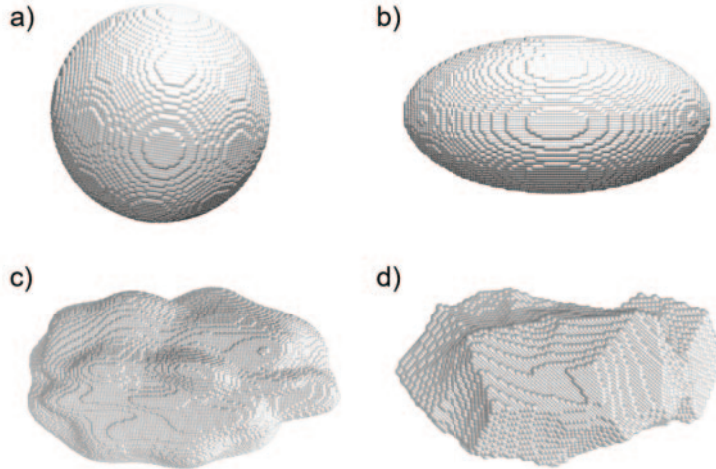
Fig. 2. – Discretised representation of the morphologies considered in this study; the particles shown here have the same volume-equivalent diameter. (a) Sphere; (b) prolate ellipsoid (axis ratios $b/a = 0.5$, $c/a = 0.4$); (c) smooth particle generated by summing spherical harmonics; (d) particle generated with an edgy *metaballs* algorithm. Asymmetric particles are chosen with the same aspect ratio as the ellipsoid.

the interactions between all the dipoles in the volume. We used the open-source code ADDA [39], which is being actively developed (`https://github.com/adda-team/adda`). With this code, we also computed the internal electric field [40]. To quantify the deviations from Lorentz-Mie scattering (spheres), we compared the experimental results to spherical particles and prolate ellipsoids (see fig. 2). In addition, to achieve a closer resemblance to the irregularly shaped particles found in the samples, we generated asymmetric morphologies by randomly deforming an ellipsoid to obtain smooth, pebble-like, or coarse shapes. The former kind of particles was obtained by summing spherical harmonics with random coefficients that vanish as their degree increases; the latter with a modified *metaballs* algorithm based on a sharp cut-off metric, to mimic the sharp edges of the particles. The refractive index of the particles in the simulations was set to $n = 1.54 + i10^{-3}$, a value close to the most common minerals found in the site [24]. A small imaginary part was included to take into account absorption due, for example, to iron oxides [41]. The number of dipoles was chosen to ensure that their size was much smaller than both the wavelength and any structural lengths of the scatterer, according to the guidelines in [39].

3. – Results

Before discussing the experimental findings for samples containing mineral dust, we report the results relating to an emulsion of micrometric droplets of kerosene and water. This sample serves as a good illustration of the scattering by spherical particles. Moreover, when drilling fluids are employed, traces can sometimes be found as contaminating residues in the meltwater samples. While the outer part of the ice cores is discarded to extract only pristine uncontaminated ice, fissures or highly porous sections may still drive part of the fluid inwards. Precautions are required to avoid altering significantly the signal from the aerosol content.
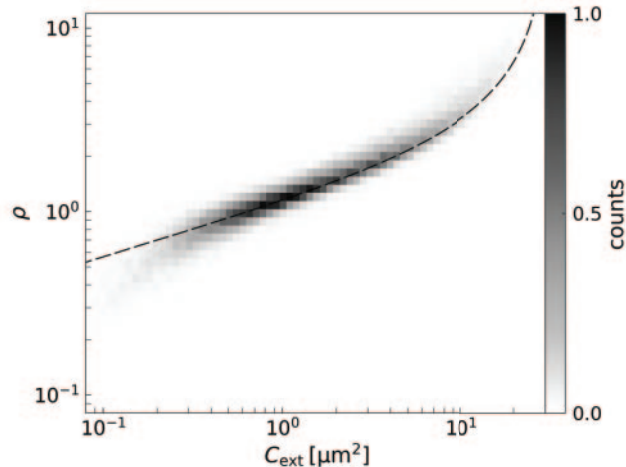
Fig. 3. – Scattering data (extinction cross-section, C_{ext} and optical thickness, ρ) for an emulsion of spherical droplets of kerosene in water reported as a two-dimensional histogram. Counts are normalised on their maximum (black). A good agreement is found with Mie calculations for $n = 1.46$, reported with a dashed line.

There are several features worth noting in this laboratory example (fig. 3). For instance, polydispersity results in an extinction cross-section distribution covering almost two orders of magnitude, while the optical thickness of the particles, at any given value of C_{ext}, lies within a much narrower range (vertical sections). This indicates that the particles are isometric (aspect ratio approaching 1), as expected by a distribution of spherical droplets, only slightly deformed by the shear stress in the cell. In the following, however, we will see that this is not a unique characteristic distinguishing spheres only. Here, data are compared with Mie calculations for spheres with a refractive index $n = 1.46$ (black dashed line in the figure, volume-equivalent diameters range $0.4 < d < 3\,\mu\text{m}$) with good agreement.

We now move on to Antarctic samples, an example of which is given by sample DB560.20-40 from Dome B ($77°\ 05'$ S, $94°\ 55'$ E) in fig. 4. In this sample, we can observe many features that are representative of this section of the Dome B ice core ($\sim$500–700 m deep), the most prominent being particle non-sphericity. Dust particles with large aspect ratios are expected from large desert sources [42, 24]; this deviation was found to have a larger effect than that of the refractive index.

For our purposes, non-isometric particles differ from spherical particles in that the field they scatter is susceptible to a change in orientation, so they produce a different distribution. Under high-shear conditions, however, it is possible to force prolate particles to rotate on a plane orthogonal to the optical axis [43]. As a result, the optical thickness is almost independent of orientation and primarily depends on the aspect ratio of the particles. As previously stated, such a system would give a 2D distribution resembling the one shown in fig. 3. Nevertheless, fitting the data with a distribution of spheres would not match the actual refractive index of the prolate particles, since these are located lower in the (C_{ext}, ρ)-plane.

Both flattened and elongated ellipsoids are present in the samples; here we discuss the latter kind. Due to the variability in particle shapes, the distribution shown in fig. 4
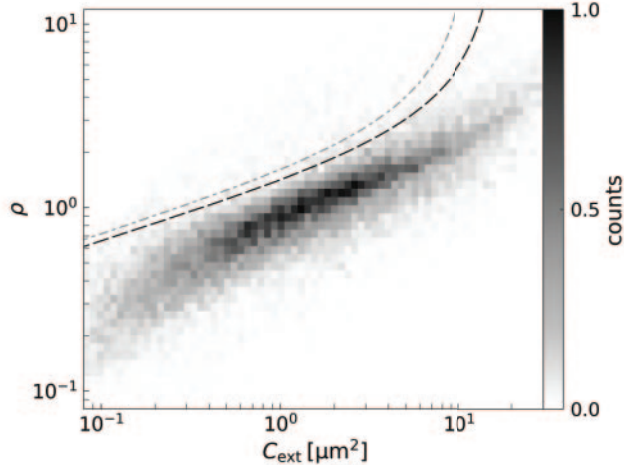
Fig. 4. – Data from sample DB560.20, containing both oblate and prolate particles. The latter have an aspect ratio 2–3. Dashed and dash-dotted lines indicate spheres with $n = 1.51$ and $n = 1.55$, respectively.

is characterised by a considerable width in both directions. While it is not possible to strictly separate the contributions from prolate and oblate particles, a thin ridge corresponding to prolate particles can be noted in the upper part of the graph, which also appears in neighbouring samples. We estimate the average aspect ratio of these particles by comparison to simulations generating a distribution of polydisperse prolate particles similar to the ones in fig. 2. Data is best described by a ratio between the major and minor axes ranging from 2 to 3. Dashed and dash-dotted lines indicate Mie scattering results for spheres of ranging diameter with $n = 1.51$ and $n = 1.55$, respectively. The whole distribution lies significantly lower in the plane. Compared to spheres (fig. 4), the distribution is also broader in the vertical direction (ρ) due to the presence of flat particles[1]. Overall, we cannot interpret data in terms of homogeneous spheres, since we would find no match with the mineralogy in any range of the particle dimension and we would, therefore, considerably overestimate the size of the particles. An example of this is given in the next section.

Let us briefly discuss the insights that can be drawn from considering the DDA simulations in some detail. In fig. 5, we compare three different elongated particles to the volume-equivalent sphere considering the case with a volume-equivalent diameter set to $d_{\mathrm{vol}} = 2.6\,\mu\mathrm{m}$. The sections show the square modulus of the internal electric field in arbitrary units.

While the three elongated particles ((b), (c), and (d)) all have similar radiative properties, they deviate from their spherical approximation (a). Similarly, the extinction cross-sections of the particles in fig. 5 are $C_{\mathrm{ext,b}} = 26.1\,\mu\mathrm{m}^2$, $C_{\mathrm{ext,c}} = 26.2\,\mu\mathrm{m}^2$, $C_{\mathrm{ext,d}} = 25.4\,\mu\mathrm{m}^2$, to be compared with $C_{\mathrm{ext,a}} = 15.4\,\mu\mathrm{m}^2$ of the corresponding volume-equivalent sphere. These values would give an extinction-equivalent diameter

---

[1] Retrieving the average aspect ratio of such oblate particles is also possible but is beyond the scope of the present paper.
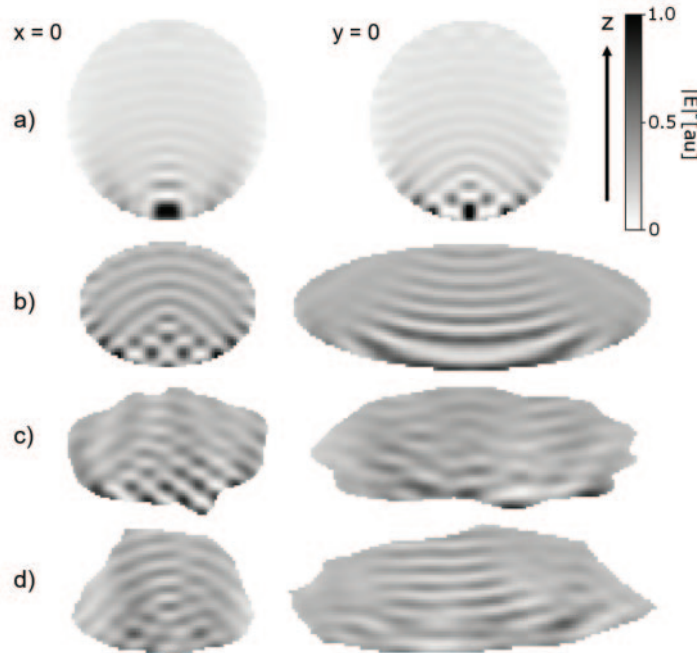
Fig. 5. – Two orthogonal sections of the particles shown in fig. 2 showing the square modulus of the internal electric field. Compared to fig. 2, sections are perpendicular to the page. For graphical convenience, the normalisation for spheres differs from the other particles. Scale factor (a): 8; (b), (c) and (d) 3. The arrow (z-axis) indicates the direction of propagation of the incoming wave; its length corresponds to $2\,\mu$m scale bar.

$d_{\mathrm{ext}} \simeq 4.1\,\mu$m. Interestingly, inverting the 2D data (C_{ext}, ρ) with a lookup table based on the Mie model would give $d_{\mathrm{LUT}} \simeq 3.3\,\mu$m and an effective refractive index $n_{\mathrm{eff}} \simeq 1.42$.

A particle small with respect to the wavelength (Rayleigh regime) exhibits an almost homogeneous internal electric field, and many approximations can be successfully made regardless of its shape [35]. Being much larger, the particles in fig. 5 exhibit a considerable variability. Averaged on the whole volume of the corresponding particles, the local fields for the specific orientation shown here are $\langle E_{\mathrm{a}} \rangle = 1.11 \pm 0.53$, $\langle E_{\mathrm{b}} \rangle = 0.96 \pm 0.27$, $\langle E_{\mathrm{c}} \rangle = 0.94 \pm 0.23$, and $\langle E_{\mathrm{d}} \rangle = 0.94 \pm 0.25$. It should be noted, in fact, that orientation with respect to the incoming wave also affects the local field considerably and in turn the overall response of a particle to radiation. Such deviations suggest that the polarizability is often an ill-defined quantity. More broadly, the three elongated morphologies exhibit a similar response to electromagnetic waves over the whole C_{ext} range; the same holds when considering the orientation of their major axis. In the present case, the surface roughness plays a secondary role, thus, it is safe to roughly describe the particles in the sample as being mainly characterised by the ratio between their axes.

Finally, we briefly discuss a sample from the EPICA(^{2}) ice core drilled at Dome C at approximately $3\,$km depth (East Antarctica, 3233 m a.s.l, 75° 06′ S; 123° 21′ E). As discussed in more detail in [37], a significant fraction of aggregate particles characterises deep samples from this site: the study was designed to quantify this fraction across the

---

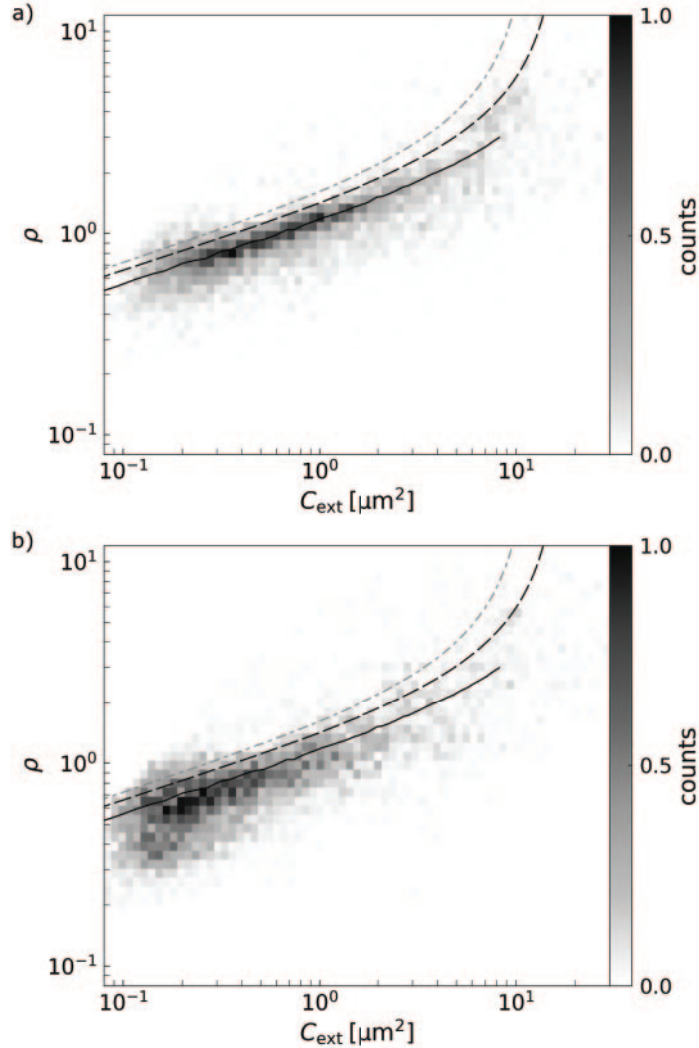(^{2}) European Project for Ice Coring in Antarctica.

Fig. 6. – (a) C_{ext}, ρ distribution for sample EDC5316, dominated by isometric aggregates of mineral dust. Solid line: distribution of porous spheres ($n = 1.54$, 0.4 void fraction); dashed line: homogeneous spheres with $n = 1.51$; dash-dotted line: homogeneous spheres with $n = 1.55$. (b) Same sample after 13 min in sonic bath.

size distribution range. Here, we briefly report the main outcomes from a geometrical standpoint (fig. 6(a)).

The aggregate particles in the samples were found to be essentially isometric, hence, the contribution of orientation as seen above can be dismissed. However, their surface roughness and abrupt internal density fluctuations due to the presence of voids differentiate them from compact spheroids. We estimated the volume fraction of the particles by comparing data with a distribution of porous isometric particles, which gives a fraction of voids ∼30–40%. The same principle is applied to set a threshold to distinguish compact from aggregate particles that alter the pristine size distribution of mineral dust in the

ice cores. As in the previous plots, we compare data to compact, homogeneous spheres: dashed and dash-dotted lines indicate spheres with $n = 1.51$ and $n = 1.55$, respectively. Only a minority of the particles are compatible with the predictions of the Mie model.

After measuring the particles, we analysed the resulting distribution after 13 minutes in a sonic bath, enough to break the aggregates. The result is shown in fig. 6(b): the centroid of the distribution is shifted towards the lower range of the C_{ext} range, as expected, and the histogram reveals the presence of small oblate particles that give a broad distribution in the vertical direction (lower-left corner of the plot).

4. – Conclusion

A key aspect that emerges from the results summarised above is that measuring two optical parameters is enough to highlight deviations from the homogeneous spherical model. Quantitatively, such deviations can compromise the outcome of inverting the scattering data to assess the particle size distribution and should, therefore, be addressed. The same also occurs when modelling the behaviour of aerosols in the atmosphere under the action of sunlight. As a first approximation, the ambiguities and inconsistencies arising from the Lorentz-Mie spherical approximation can be explained in terms of a few morphological characteristics of the particles. Experimental and numerical data obtained from a DDA algorithm show that shape and orientation are the main drivers of the scattering efficiency for the non-spherical particles in our present samples. We found that the radiative properties of elongated particles mainly depend on the ratio between their major and minor axes. High-shear conditions force particles towards preferred orientations, a constraint that can be exploited to estimate their aspect ratio. Simulations indicate that other features such as surface roughness give a second-order contribution, thus, this approximation is enough for this purpose. Similarly, we estimated the filling factor of isometric aggregates of mineral dust by comparing simulations to experimental data. Due to their peculiar structure that lowers their effective polarizability, such aggregates can be distinguished from compact particles regardless of their size.

$* \ * \ *$

REFERENCES

[1] Booth B., Dunstone N., Halloran P., Andrews T. and Bellouin N., *Nature*, **484** (2012) 7393.
[2] Ito A. and Wagai R., *Sci. Data*, **4** (2017) 170103.

[3] TEGEN I. and SCHEPANSKI K., *IOP Conf. Ser.: Earth Environ. Sci.*, **7** (2009) 012001.

[4] TEXTOR C. *et al.*, *Atmos. Chem. Phys.*, **6** (2006) 7.

[5] FIELD J. P. *et al.*, *Front. Ecol. Environ.*, **8** (2010) 8.

[6] SHAO Y., *J. Geophys. Res. Atmos.*, **106** (2001) D17.

[7] KRUEGER B., GRASSIAN V., COWIN J. and LASKIN A., *Atmos. Environ.*, **38** (2004) 36.

[8] WEIDLER P. and FRIEDRICH F., *Am. Mineral.*, **92** (2007) 7.

[9] STOCKER T. *et al.*, *Climate Change 2013: The Physical Science Basis* (Cambridge University Press) 2014.

[10] BURGOS M. *et al.*, *Atmos. Chem. Phys.*, **20** (2020) 17.

[11] TAKEMURA T., EGASHIRA M., MATSUZAWA K., ICHIJO H., O'ISHI R. and ABE-OUCHI A., *Atmos. Chem. Phys.*, **9** (2009) 9.

[12] GHAN S. and ZAVERI R., *J. Geophys. Res. Atmos.*, **112** (2007) D10.

[13] LANE P., HART M., JAIN V., TUCKER J. and EVERSOLE J., *J. Quant. Spectrosc. Radiat. Transf.*, **208** (2018) 188.

[14] MOOSMÜLLER H., CHAKRABARTY R. and ARNOTT W., *J. Quant. Spectrosc. Radiat. Transf.*, **110** (2009) 11.

[15] FERRERO L. *et al.*, *Sci. Total Environ.*, **686** (2019) 452.

[16] MÜLLER D. *et al.*, *J. Geophys. Res. Atmos.*, **115** (2010) D7.

[17] CURTIS D. B. *et al.*, *J. Geophys. Res. Atmos.*, **113** (2008) D8.

[18] CREMONESI L. *et al.*, *Aerosol Sci. Technol.*, **54** (2020) 4.

[19] WEST R., DOOSE L., EIBL A., TOMASKO M. and MISHCHENKO M., *J. Geophys. Res. Atmos.*, **102** (1997) D14.

[20] MASSABÒ D. *et al.*, *Atmos. Environ.*, **108** (2015) 1.

[21] ROMANOV A. V. and YURKIN M. A., *Laser Photon. Rev.*, **15** (2021) 2000368.

[22] HOLBEN B. *et al.*, *Remote Sens. Environ.*, **66** (1998) 1.

[23] FORMENTI P. *et al.*, *Atmos. Chem. Phys.*, **11** (2011) 16.

[24] DELMONTE B. *et al.*, *Quaternary Sci. Rev.*, **168** (2017) 55.

[25] LAMBERT F., BIGLER M., STEFFENSEN J., HUTTERLI M. and FISCHER H., *Clim. Past*, **8** (2012) 2.

[26] SVENSSON ANDERS *et al.*, *Clim. Past*, **16** (2020) 4.

[27] CLAQUIN T., SCHULZ M., BALKANSKI Y. and BOUCHER O., *Tellus B*, **50** (1998) 5.

[28] PETIT J. R. *et al.*, *EGU General Assembly Conference Abstracts*, **EGU2013** (2013) 6255.

[29] SIMONSEN M. *et al.*, *Clim. Past*, **14** (2018) 5.

[30] HEIM M., MULLINS B., UMHAUER H. and KASPER G., *J. Aerosol Sci.*, **39** (2008) 12.

[31] CUCCIA E., BERNARDONI V., MASSABÒ D., PRATI P., VALLI G. and VECCHI R., *Atmos. Environ.*, **44** (2010) 27.

[32] GINOUX P., *J. Geophys. Res. Atmos.*, **108** (2003) D2.

[33] LACK D., RICHARDSON M., LAW D., LANGRIDGE J., CAPPA C., MCLAUGHLIN R. and MURPHY D., *Aerosol Sci. Technol.*, **46** (2012) 5.

[34] LINKE C., MÖHLER O., VERES A., MOHÁCSI Á., BOZÓKI Z., SZABÓ G. and SCHNAITER M., *Atmos. Chem. Phys.*, **6** (2006) 11.

[35] VANDEHULST H., *Light Scattering by Small Particles* (Dover, New York) 1957.

[36] NOUSIAINEN T., *J. Quant. Spectrosc. Radiat. Transf.*, **110** (2009) 14.

[37] POTENZA M. A. C. *et al.*, *ACS Earth Space Chem.*, **1** (2017) 5.

[38] POTENZA M. A. C., SANVITO T. and PULLIA A., *AIP Adv.*, **5** (2015) 11.

[39] YURKIN M. A. and HOEKSTRA A., *J. Quant. Spectrosc. Radiat. Transf.*, **112** (2011) 13.

[40] HOEKSTRA A., RAHOLA J. and SLOOT P., *Appl. Opt.*, **36** (1998) 37.

[41] LAFO S., SOKOLIK I., RAJOT J. L., CAQUINEAU S., GAUDICHET A., *J. Geophys. Res. Atmos.*, **111** (2006) D21.

[42] DUBOVIK *et al.*, *J. Geophys. Res. Atmos.*, **111** (2006) D11.

[43] POTENZA M. A. C. *et al.*, *Sci. Rep.*, **6** (2016) 1.